



Numerical Modeling on Deformation of Fractured Reservoir Bank Slopes During Impoundment: Case Study of the Xiluodu Dam

Bing Liu¹ · Zhihong Zhao¹ · Sicong Chen¹ · Qiang Yang²

Received: 9 March 2023 / Accepted: 7 September 2023 / Published online: 25 September 2023
© The Author(s), under exclusive licence to Springer-Verlag GmbH Austria, part of Springer Nature 2023

Abstract

Investigating deformation behavior of fractured reservoir bank slopes during impoundment plays an essential role in safety control of high arch dams. Because of changes in water levels during impoundment, the fractures are subjected to varying water pressure and cyclic wetting–drying conditions. In this numerical study, mechanical, physical, and chemical water–rock interactions in rock fractures are incorporated into discrete element modeling of fractured reservoir bank slopes, and effects of mechanical, physical, and chemical water–rock interactions on deformation of fractured reservoir bank slopes are investigated based on a case study of valley deformation at the Xiluodu Hydropower Station. The mechanical water–rock interaction is considered by the effective stress law, while the physical and chemical water–rock interactions are modeled by some empirical deterioration laws. The results showed that the modeled and monitored deformation behaviors of fractured reservoir bank slopes are in good agreement. The slip of shear zones due to water pressure elevation and mechanical parameter weakening is the main reason of impoundment-induced valley contraction. Discrete element method considering water–rock interactions can serve as a robust and reasonable tool to predict the deformation magnitude of fractured reservoir bank slope.

Highlights

- Mechanical, physical and chemical water–rock interactions in rock fractures are incorporated into discrete element modeling of fractured reservoir bank slopes.
- Four scenarios are designed to understand the role of mechanical, physical and chemical water–rock interactions on deformation of fractured reservoir bank slopes.
- The slip of shear zones due to water pressure elevation and mechanical parameter weakening is the main reason of impoundment-induced valley contraction.

Keywords Reservoir bank slope · Rock fracture · Water–rock interaction · Discrete element method · Valley contraction

1 Introduction

Deformation or failure of fractured reservoir bank slopes induced by changes in water levels during impoundment occur in many dams worldwide (Zhao et al. 2018; Wu et al. 2021; Zhou et al. 2022; Zhou et al. 2023). In 1959, the failure of the left bank abutment of the Malpasset dam after 5

years of reservoir operation was the first failure of an arch dam (Londe 1987). In 1963, the southern bank slope of the Vajont dam failed and then thrust onto the opposite bank after the reservoir was filled to about 2/3 (Müller-Salzburg 1987; Paronuzzi et al. 2013). In the 1960s, a deep-seated gravitational slope deformation was present on the left bank slope of the Beauregard dam after reservoir filling (Barla et al. 2010). In the past 2 decades, more than 300 landslides were triggered or reactivated after initial impoundment in the Three Gorges dam (Yin et al. 2016). In addition, valley contractions were monitored at the Xiluodu, Jinping-I, Jiangya, Laxiwa, Tongjiezi, and Baihetan dams in China after the initial impoundments (Cheng et al. 2017; Liu et al. 2020; Sun et al. 2020; Zhou et al. 2022; Li et al. 2023a, b;

✉ Zhihong Zhao
zhzhao@tsinghua.edu.cn

¹ Department of Civil Engineering, Tsinghua University, Beijing, China

² Department of Hydraulic Engineering, Tsinghua University, Beijing, China

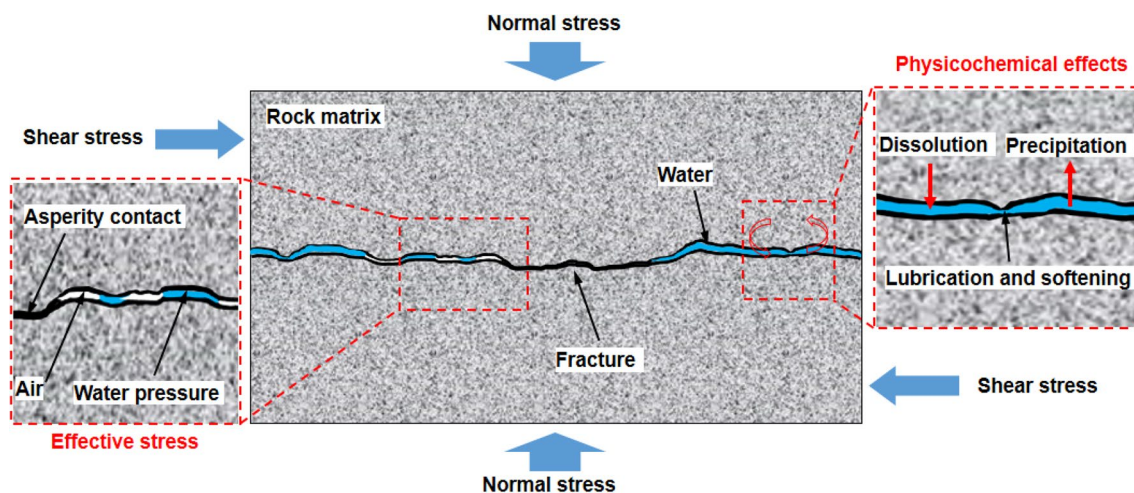


Fig. 1 Schematic diagram of water–rock interactions in a single rock fracture

Xu et al. 2023). For example, the magnitude of valley contraction in the Xiluodu dam was up to 70–80 mm after 9 year impoundment (2012–2021). It is recognized that many factors including in-situ stresses, reservoir pressure, and creep and water–rock interactions control the deformation behavior of reservoir bank slopes (Sun et al. 2018; Zhao et al. 2018; Xia et al. 2019; Jiang et al. 2020; Li et al. 2022; Wu et al. 2021; Li et al. 2022; Zhou et al. 2022; Li et al. 2023a, b; Zhuang et al. 2023), but predicting deformation magnitude of reservoir bank slope is still a challenging task due to the complexity and uncertainty of water–rock interactions.

Continuum-based numerical modeling is used to simulate deformation of reservoir bank slopes subjected to changes in water levels (Paronuzzi et al. 2013; Liu et al. 2018; Xiong et al. 2019; Liu et al. 2020; Chen et al. 2022; Yang et al. 2022a, b; Li et al. 2023a, b; Xu et al. 2023; Zhuang et al. 2023). Based on the generalized effective stress principle for rock masses, Cheng et al. (2017) and Wang et al. (2020) used 3D parallel nonlinear elasto-plastic finite-element code TFINTE to model slope deformation toward the river and valley contractions of the Jinping-I high arch dam. Zhou et al. (2022) developed coupled two-factor stress-deformation-seepage model to simulate the valley deformation of the Xiluodu dam. It is known that continuum-based numerical model can represent the equivalent mechanical and hydraulic properties of reservoir bank slopes including multi-scale fractures. Note that there are many discontinuities of different scales in the reservoir bank slopes, and those discontinuities usually play an important role in deformation or failure of reservoir bank slopes during impoundment (Wu et al. 2021). Therefore, discrete element method (DEM), which can explicitly represent multi-scale fractures, has been increasingly used to simulate the stability of fractured reservoir bank slopes subjected to water–rock interactions

(Farinha et al. 2012; Espada et al. 2018; Zhao et al. 2018; Sun et al. 2023).

Introduction of water into rock fractures modifies the mechanical properties of fractured rock masses through mechanical, physical, and chemical ways (Pellet et al. 2013; Qiao et al. 2016; Zhao et al. 2017a, b; Kim and Jeon 2019; Li et al. 2020; Pirzada et al. 2020; Dou et al. 2020, 2021; Shang et al. 2020; Yin et al. 2020; Fan et al. 2022; Fig. 1). The mechanical water–rock interaction means the reducing normal stress due to water pressure, i.e., the effective stress principle (Biot 1941; Zhao et al. 2021). The physical water–rock interaction includes lubrication, softening, and argillization, which induces reduction in basic friction angle and asperity strength (Dou et al. 2020). The chemical water–rock interaction includes dissolution, precipitation, ion exchange, hydration, and corrosion, which is time-dependent (Dou et al. 2021). However, the above three types of water–rock mechanical interactions have not been fully considered in the previous numerical modes of fractured reservoir bank slopes (Zhao et al. 2018).

The main aim of this numerical study is to understand the roles of mechanical, physical, and chemical water–rock interactions in deformation of fractured reservoir bank slopes based on a case study of the Xiluodu dam. Mechanical, physical, and chemical water–rock interactions in rock fractures are first incorporated into DEM modeling, and then, the DEM model of the reservoir bank slopes of the Xiluodu dam is built and calibrated based on the monitoring data of valley contraction. Four scenarios considering different water–rock interactions are compared to uncover the mechanisms of valley contraction of the Xiluodu dam during impoundment. Compared with the authors' previous numerical study on deformation behavior of fractured reservoir bank slopes (Zhao et al. 2018), the contributions of this study include the following three aspects: 1) effective

stress coefficient is considered to describe the water–rock mechanical interaction in rock fractures; 2) an empirical model is used to describe the weakening of rock fractures subjected to long-term water–rock chemical interaction; 3) two-dimensional (2D) DEM model is extended to three-dimensional (3D) one.

2 Methods

2.1 Water–Rock Interaction in Rock Fracture

Mechanical, physical, and chemical water–rock interactions in rock fractures (Fig. 1) are separately considered in DEM modeling.

(1) Mechanical water–rock interaction

The reducing normal stress due to water pressure in rock fracture makes fracture slip more easily according to effective stress principle (Biot 1941; Zhao et al. 2021)

$$\sigma'_n = \sigma_n - \alpha p, \tag{1}$$

where σ_n is the total normal stress, σ'_n is the effective normal stress, p is the water pressure in fracture voids, and α is effective stress coefficient. Note that α can be regarded as the ratio of the fracture surface supported by water pressure to the whole fracture surface (Fig. 1). For rough rock fractures, Zhao et al. (2021) proposed an expression of α based on the maximum fracture closure (u_{nmax}) and the initial normal stiffness (k_{n0})

$$\alpha = \begin{cases} \frac{1}{1 + \frac{\sigma_n - p}{k_{n0} u_{nmax}}} & \sigma_n \geq p \\ 1 & \sigma_n < p \end{cases}. \tag{2}$$

(2) Physical water–rock interaction

Li et al. (2020) showed that water-mediated lubrication is the primary mechanism reducing the shear parameters of rock fractures in crystalline rocks, and thus, the fracture friction angle and cohesion of rock fractures are reduced by a certain degree to consider the weakening effect due to physical water–rock interaction (Zhao et al. 2018). Note that the fracture friction angle and cohesion of rock fractures which are subjected to periodic wetting and drying recover to their initial values during drying, i.e., water-level reduction (Zhao et al. 2017a).

(3) Chemical water–rock interaction

Dou et al. (2021) conducted an experimental study on reductions in shear parameters of rock fractures due to long-term water–rock chemical interaction, and provided the empirical evolution models for the shear parameters with immersion duration (t)

$$\tau_p = \tau_{p0} (1 - w_p \ln(t + 1)) \tag{3a}$$

$$\tau_r = \tau_{r0} (1 - w_r \ln(t + 1)) \tag{3b}$$

$$k_s = k_{s0} (1 - w_k \ln(t + 1)), \tag{3c}$$

where τ_p , τ_r , and k_s are the peak shear strength, residual shear strength, and shear stiffness, τ_{p0} , τ_{r0} , and k_{s0} are the initial peak shear strength, residual shear strength, and shear stiffness before immersion, and w_p , w_r , and w_k are the material parameters. The three material parameters w_p , w_r , and w_k are 0.081, 0.028, and 0.112, respectively, and the unit of immersion duration is month. Therefore, the evolution of shear parameters of those rock fractures always below water level follows Eq. (3) during long-term immersion. Note that material parameters determined in Dou et al. (2021) may or may not be directly used in practical engineering, and more experiments are needed to determine the material parameters for basalt fractures in future studies.

2.2 DEM Modeling

A 3D distinct element code (3DEC version 5.2) is adopted in this study (Itasca 2016). Rock blocks are divided into deformable and elastic zones, and the mechanical response to external loading is determined by Young’s modulus (E) and Poisson’s ratio (ν). Considering that permeability of intact rock is much lower than that of rock fractures, rock blocks are assumed to be impermeable, and fluid flow only occurs through rock fractures. After impoundment, the weight of the reservoir water is simulated by applying the water pressure corresponding to the water level to the reservoir bottom and slope surfaces. Both fluid flow and mechanical deformation are assumed to enter a new steady state after water-level changes.

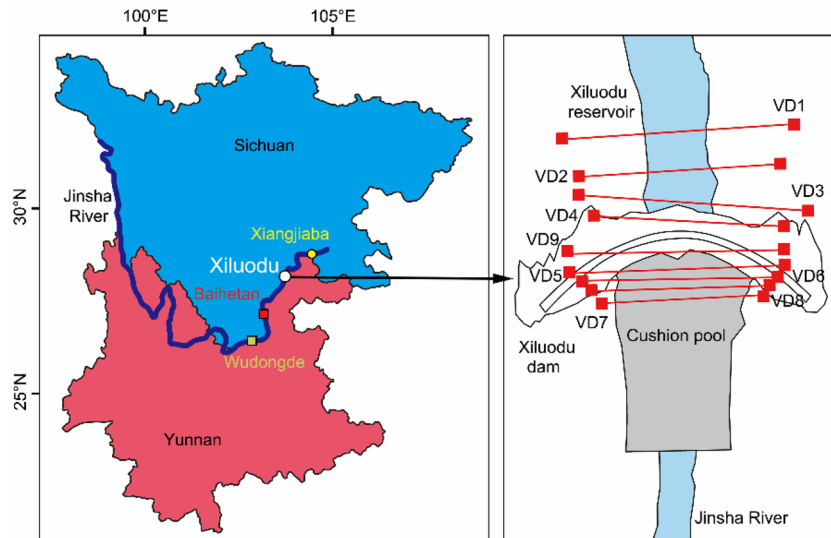
Rock fracture were regarded as an aggregate of contact elements between two rock blocks. Effective normal stress (σ'_n) and shear stress (τ_j) increments in each contact element are calculated as follows:

$$\Delta\sigma'_n = -k_n \Delta u_n \tag{4}$$

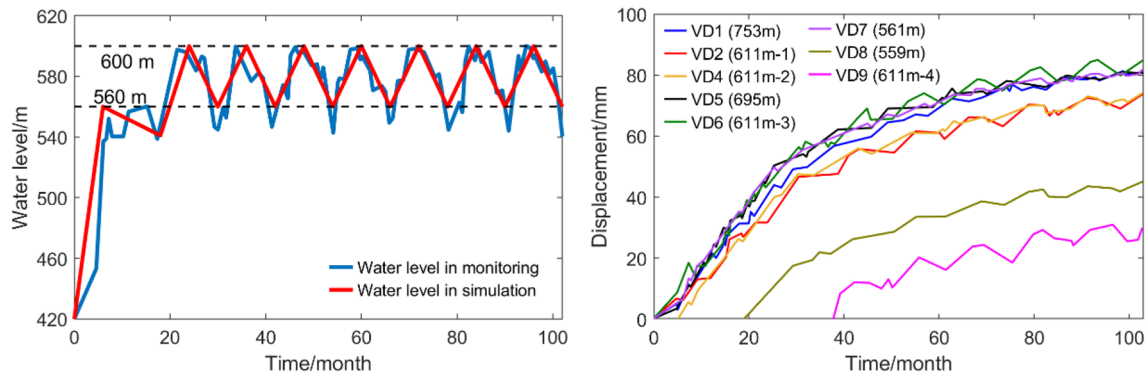
$$\Delta\tau_j = -k_s \Delta u_s, \tag{5}$$

where k_n , Δu_n , and Δu_s are normal stiffness, normal displacement increment, and shear displacement increment, respectively. Beyond the elastic range, the stress increments were limited by tensile and shear strengths, defined by Mohr coulomb-slip joint model

$$\sigma_j^t = -T_j \tag{6}$$



(a) Geological condition



(b) Water level

(c) Valley deformation

Fig. 2 Geological condition and measured water levels of valley deformations in the Xiluodu reservoir (after Li et al. 2023b)

$$\tau_j = c_j + \sigma'_n \tan \phi_j (\text{before failure}) \quad (7)$$

$$\tau_j = \sigma'_n \tan \phi_r (\text{after failure}), \quad (8)$$

where T_j , c_j , ϕ_j , and ϕ_r are the tensile strength, cohesion, friction angle, and residual friction angle of rock fractures.

Under the assumptions of smooth parallel plates, impermeable boundaries, and incompressible fluid, fluid flow in rock fractures is described by the cubic law (Zhao et al. 2018; Liu et al. 2023a)

$$q = -ka^3 \frac{\Delta p}{l}, \quad (9)$$

where q is the fluid flow rate, $k = 1/12\mu$ is the fracture permeability factor, a is the fracture aperture, Δp is the fluid

pressure difference, l is the fracture length, and μ is the fluid viscosity. Note that effects of rough fracture surfaces and infilled materials are not considered in this study.

3 Case Study of Valley Contraction in the Xiluodu Reservoir

3.1 Engineering Geological Condition

The Xiluodu dam, which is a double-curved arch dam with a crest elevation of 610 m and a height of 285.5 m, is at the lower reaches of the Jinsha River, Yunnan province, China (Fig. 2a). The Xiluodu dam is located in the center of the Yongsheng tectonic basin, and the river valley in the dam site area is U-shaped. The valley is deeply incised, and the

hilltops are up to 2000 m above the valley. The strata incline to the downstream left bank at an angle of 3–5°, and the main weak discontinuities are the 13 shear zones developed between the basalt layers (from $P_2\beta_1$ to $P_2\beta_{14}$) due to tectonic shearing (Li et al. 2023a, b). Some layers were thin, limiting the formation of grid. To avoid the dimension of grid exceeding the thickness of layer, two or three adjacent thin layers ($P_2\beta_1 \sim P_2\beta_2$, $P_2\beta_4 \sim P_2\beta_5$, $P_2\beta_7 \sim P_2\beta_8$, $P_2\beta_9 \sim P_2\beta_{11}$) were combined into one single layer for easy gridding of the numerical model (Fig. 3). The shear zones are infilled with basalt breccia and fragments, and thus have low mechanical parameters. Due to the fact that the thickness (about 0.45–0.7 m) of the shear zones is much lower than the valley depth, the surface roughness and infilled materials cannot be explicitly considered in numerical modeling. The shear zones are termed and considered as fractures in numerical modeling for simplicity. Because the limestone formation is below the basalt formation, the dissolution of limestone caused by groundwater flow may not be a significant factor compared with weakening of the shear zones in the basalt formation. Karstification is not considered in the present modeling.

The impoundment process of the Xiluodu reservoir is divided into two phases (Fig. 2b). The first impoundment phase lasted for about 18 months (December 2012–May 2014), during which the water level quickly rose from 420 to 560 m and fluctuated between 540 and 560 m. The second impoundment phase started in May 2014, and the maximum water level reached 600 m in October 2014. After that the reservoir water level cycled between the maximum water level of 600 m during rainy season and low water level of 550 m during dry season. From May 2014 to June 2021, the Xiluodu reservoir has experienced seven periodic changes in water levels. Nine survey lines VD1–9 with elevations from

561 to 753 m were arranged to monitor valley deformation due to impoundment (Fig. 2a); among them, the seven survey lines VD1–7 were initiated to monitor valley deformation in May 2014 and the other two survey lines VD8–9 were initiated after the first impoundment phase (Fig. 2c).

3.2 Numerical Model and Calibration

The numerical model is about 800 m in height, 1660 m in width, and 1000 m in length (Fig. 3). Li et al. (2023b) showed that the valley contractions are almost the same at the upstream and downstream locations, and the valley contraction is mainly caused by slip along the weak fault and shear zones below the dam foundation after reservoir impoundment. Therefore, the arch dam interaction may be neglected for computational simplicity, and the arch dam was not considered in the present numerical model. The possible arch dam interaction is discussed in Sect. 4.3. Roller boundaries were assigned on the left and bottom boundaries of the model. Generally, the distance between the boundary and slope surface should be sufficiently far to avoid boundary effect, but this increases the number of zones and the calculation time. To allow the slip to occur between the different blocks, the right boundary above C3 was set as constant stress boundary. Before impoundment the stress state of the zones along the right boundary was stored, and then remained the constant value during impoundment. All boundaries except the outcrop of rock fractures were set to be impermeable, but the lateral boundaries of the shear zones were set as constant water levels. The parameters of rock blocks, fractures, and fluid in mechanical model and hydraulic model are given in Table 1. The water–rock interactions have different effects on shear parameters of different rock fractures depending on the positions of rock fractures

Fig. 3 Numerical model, boundary condition, and representative survey lines for the Xiluodu reservoir. Some adjacent thin layers ($P_2\beta_1 \sim P_2\beta_2$, $P_2\beta_4 \sim P_2\beta_5$, $P_2\beta_7 \sim P_2\beta_8$, $P_2\beta_9 \sim P_2\beta_{11}$) are combined into one single layer for easy gridding of the numerical model

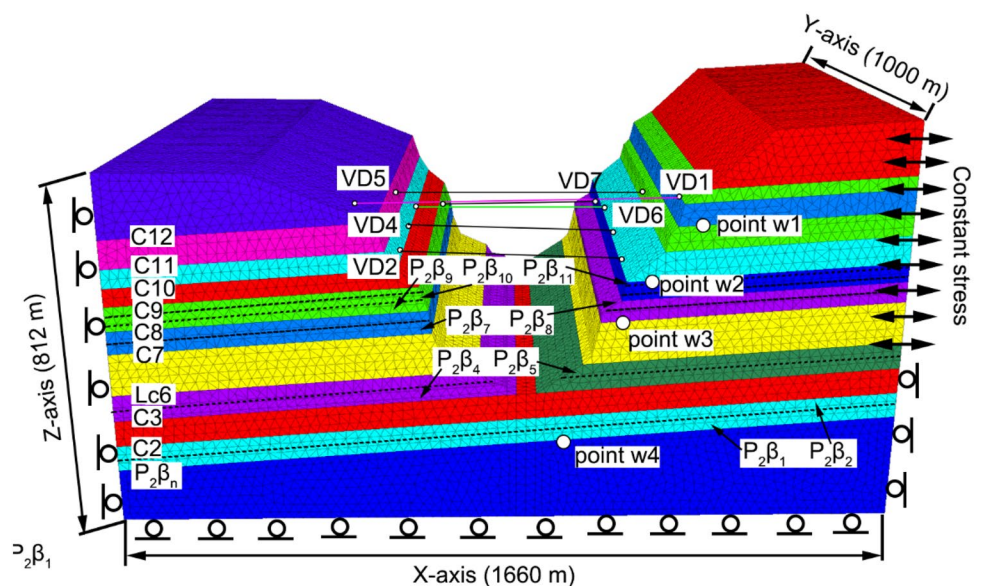
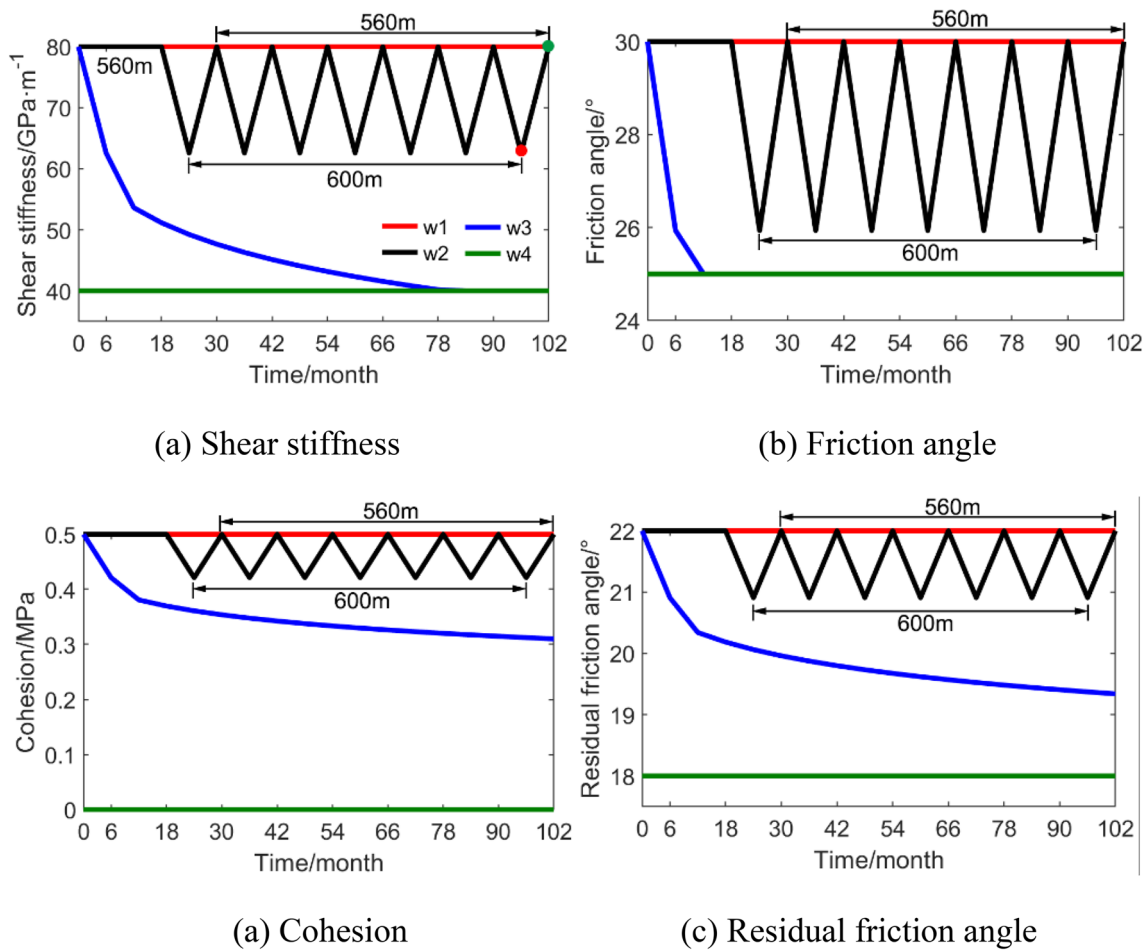


Table 1 Parameters of rock mass and faults

Category	Properties	Initial value	Minimum value
Rock block	Young's modulus (GPa)	9	9
	Poisson's ratio	0.25	0.25
	Density (kg/m^3)	2700	2700
Fluid	Bulk modulus (GPa)	2	2
	Density (kg/m^3)	1000	1000
	Viscosity (Pa·s)	0.0005	0.0005
Discontinuities	Initial normal stiffness (GPa/m)	80	–
	Maximum fracture closure (m)	0.4e-3	–
	Normal stiffness (GPa/m)	80	80 (40)
	Shear stiffness (GPa/m)	80	40
	Cohesion (MPa)	0.5	0
	Friction angle ($^\circ$)	30	25
	Residual friction angle ($^\circ$)	22	18
Tensile limit (MPa)	0	0	

**Fig. 4** The relation between shear stiffness, friction angle, cohesion, and the residual friction angle of the points w1 ~ w4 (see Fig. 3) and impundment duration

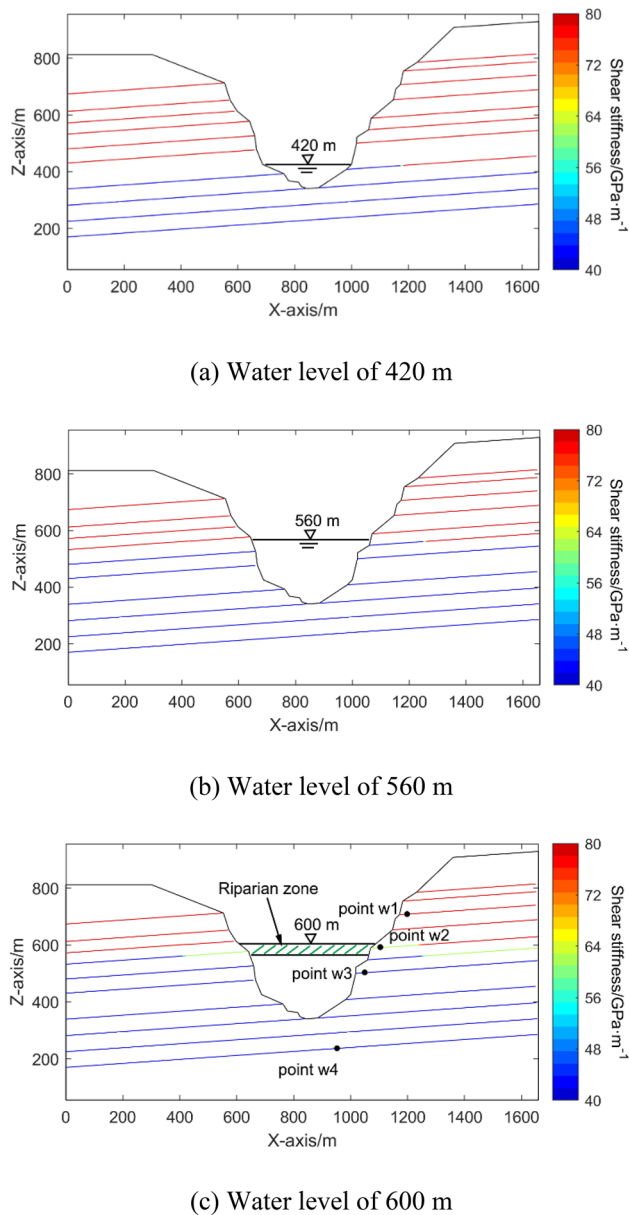


Fig. 5 Distributions of shear stiffness of the faults under different water levels

(Fig. 4). For those fractures below the initial water level of 420 m (e.g., point w4 in Figs. 3 and 5c), they have the lowest shear parameters including shear stiffness, peak shear strength (friction angle and cohesion), and residual shear strength (residual friction angle). For those fractures below the water level of 560 m (e.g., point w3 in Figs. 3 and 5c), their shear parameters decrease according to Eq. (3). For those fractures between the water levels of 560 m and 600 m (e.g., point w2 in Figs. 3 and 5c), their shear parameters decrease and recover during rainy and dry seasons, but the cohesion becomes zero and the residual friction angle is applied once slip occurs. For those fractures above the water

level of 600 m (e.g., point w1 in Figs. 3 and 5c), they have the highest shear parameters. Taking the shear stiffness as an example, Fig. 5 shows the distributions of shear stiffness of the fractures under the water levels of 420 m, 560 m, and 600 m, respectively.

The initial state before impoundment was achieved by the three calculation stages under gravity and initial water level of 420 m: (1) elastic solution without water, (2) elastic solution under initial water level of 420 m, and (3) full solution under water level of 420 m. The obtained in-situ stresses are similar to the measured values in Yang et al. (2022a, b). To enhance simulation efficiency, the practical impoundment process (blue curves in Fig. 2b) was simplified as regular changes in water levels (red curves in Fig. 2b). For each cycle of water-level change during impoundment, the calculation included three steps after fluid flow calculation: (1) adjusting the shear parameters of rock fractures, (2) determining the effective stress coefficient α of rock fractures, and (3) mechanical calculation. The data of survey lines VD1-7 are used to calibrate the built numerical model and monitoring points are presented in Fig. 3.

Figure 6 shows the distributions of water pressure and effective stress coefficient under the water levels of 560 m and 600 m in the reservoir bank slopes. For the segments of rock fractures close to the slope surface, α was close to 1. For each fracture, α decreased with the distance between the segment and the slope surface increasing. This phenomenon was related to the distribution of normal stress. For the segments close to the slope surface, the normal stress was small due to the small depth of upper rock strata. For the segments at a distance from the slope surface, the normal stress got larger with depth of upper rock strata increasing. Under the different water level, α also changed, as shown in Fig. 6b.

Figure 7 shows the comparison between the monitoring data and the numerical results. Figure 8 shows the displacement vectors and X-displacement of rock mass and shear displacement of rock fractures. For both the right and left bank slope, the displacement of the valley was large for the left and right slope toe between the key segments of C3 and Lc6. The main direction of displacement vectors was upward at the bottom of the reservoir, which was related to the water pressure in rock fractures. Except for the slope toe between the key segments of C3 and Lc6, the magnitude of the displacement vectors in the right bank slope was relatively larger than that in the left bank slope. This phenomenon was also observed by field observation (Liu et al. 2020) and it might be related to inclination of the strata dipping to left bank at an angle of 3~5°, which caused rock mass easily slip along discontinuities in the right bank. For both the left and right bank slope, the displacement vectors of the whole rock blocks mainly pointed toward the reservoir. For survey lines with elevations of 561 m and 695 m, the valley contractions were 87.3 and 80.7 mm, respectively.

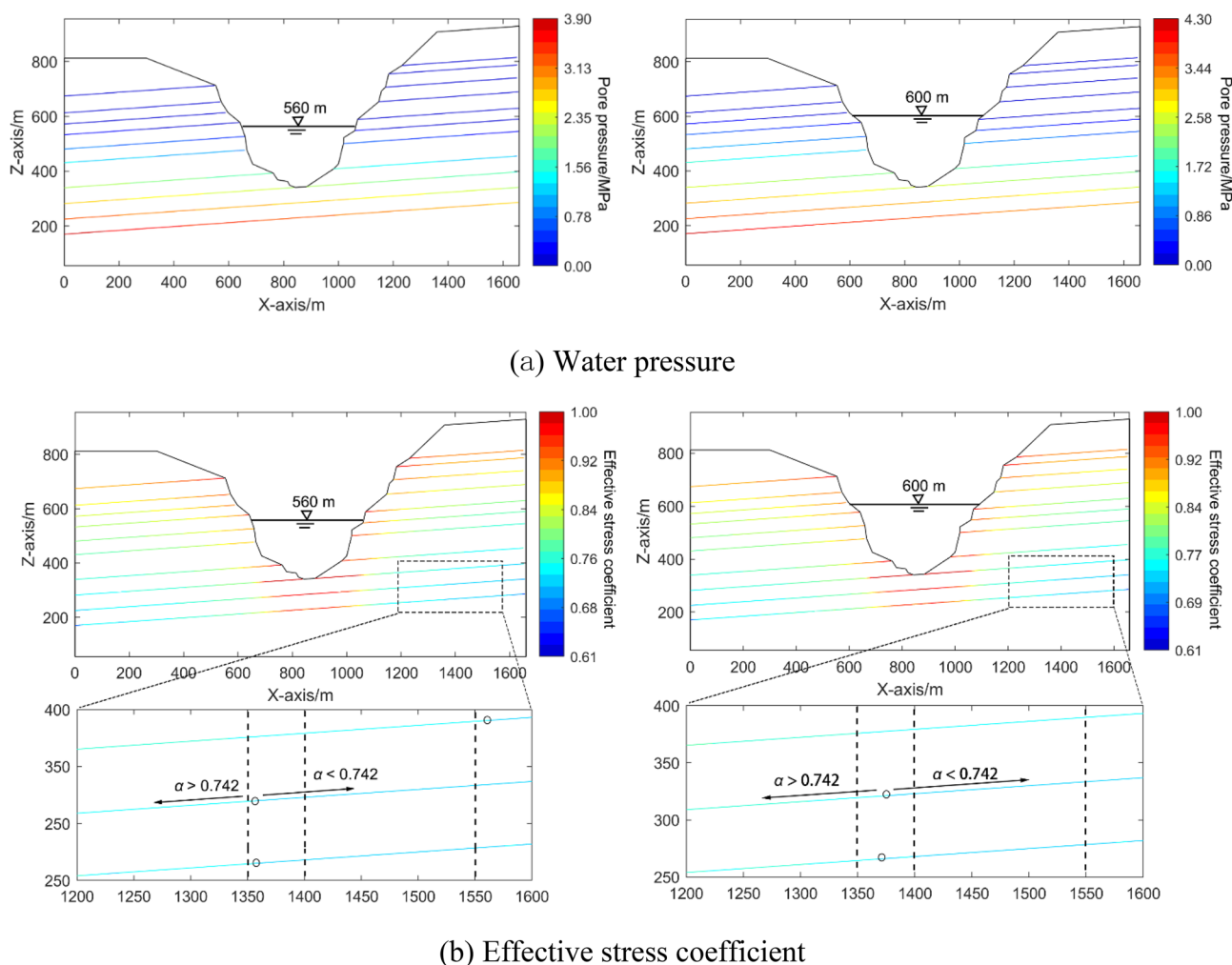


Fig. 6 Distributions of water pressure and effective stress coefficient in the reservoir bank slopes under different water levels

3.3 Numerical Scenarios and Results

Based on the calibrated numerical model in Sect. 3.2 (referred as Scenario I), the other three scenarios are designed to understand the role of mechanical, physical, and chemical water–rock interactions on deformation and stability of fractured reservoir bank slopes. In Scenario I, both reduction of mechanical parameters (Step 1) and updating of α (Step 2) were conducted. In Scenario II, only reductions in shear parameters of rock fractures (Step 1) were conducted, but α did not change with changing water pressures. In Scenario III, only updating of α (Step 2) was conducted, but reductions in shear parameters of rock fractures were neglected. In Scenario IV, reduction in normal stiffness of rock fractures was further added into the case of Scenario I, and the ratio of normal stiffness to shear stiffness was assumed to be a constant. Considering that u_{nmax} was related to the normal stiffness, $u_{nmax} \cdot k_{n0}$ was treated as a certain value in Eq. (2).

Figure 9 shows the magnitude of fracture shear displacement measured along the line with $y = 500$ m and the curves of fracture shear displacement versus X-coordinate in the right reservoir banks in different scenarios. For Scenario I, significant shear displacements occur along the fractures C3–C7 and the maximum value was about 263 mm in Fig. 12a. In this study, the fracture segment with shear displacement larger than 50 mm is defined as the key segment, which means that significant slip occurs along the fracture. The length of the key segments is denoted as W_{50} , which serves as an index to evaluate rock strata slipping toward the reservoir along rock fractures. The coordinates and lengths of key segments are shown in Table 2. The key segments of C3 were in the range of 651 to 856 m and 902 to 1155 m and W_{50} were 205 and 253 m in the left and the right banks, respectively. The key segments of Lc6 were in the range of 647 to 780 m and 1005 to 1135 m in the left and right banks, respectively.

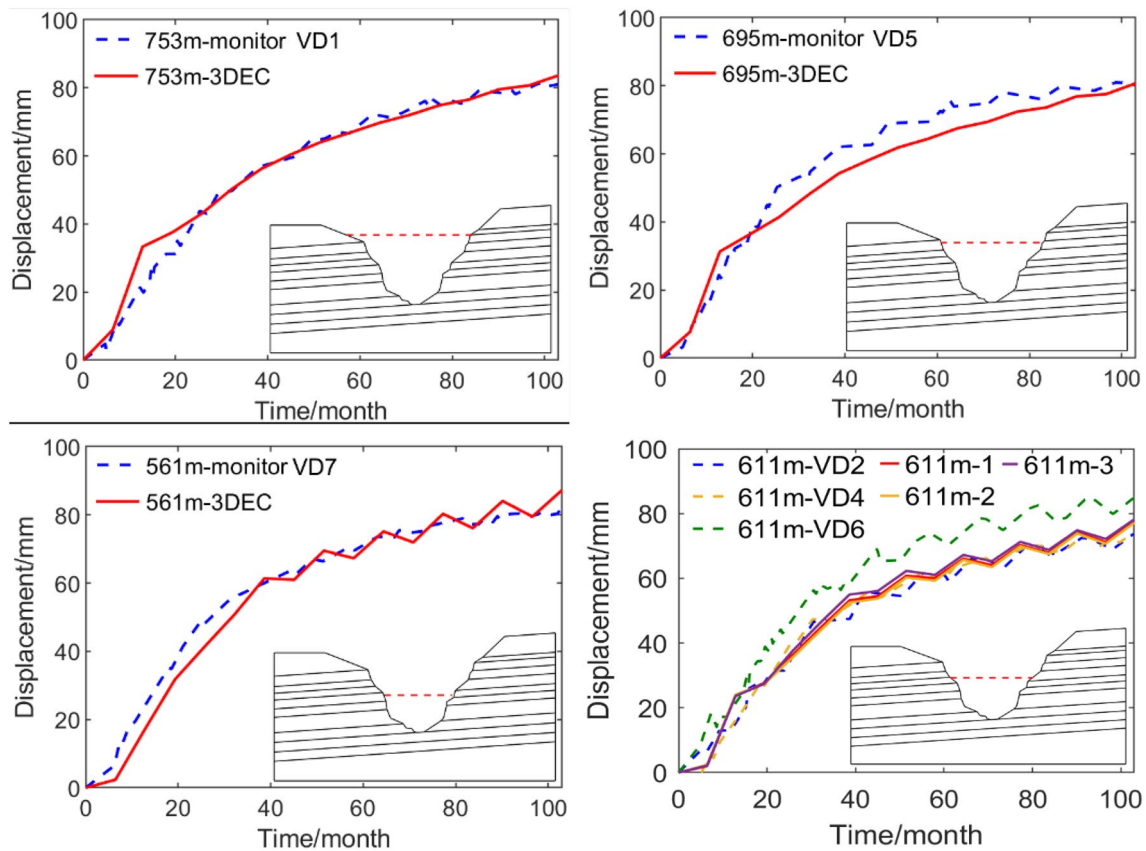


Fig. 7 Comparison of deformation of valley width between monitoring and numerical simulation

In Scenario II, $\alpha = 1$ was considered in all the rock fractures. The direction of displacement vectors in Scenario II was similar to that in Scenario I, while the magnitude was relatively larger (Fig. 10b). Compared with Scenario I, the valley contraction was 96.3 mm and 87.5 mm in the elevations of 561 m and 695 m, increasing by 10.3% and 8.4% (Fig. 11b), the larger fracture slips also occurred along the fractures C3~C7 (Fig. 12a, b). For two bank slopes, the sums of W_{50} for C3~C7 was 10 m, 7 m, and 6 m larger than the values in Scenario I (Table 2). Considering $\alpha = 1$ decreases the effective normal stress more significantly along rock fractures and made the fracture slip easily, which may overestimate the valley contraction.

In Scenario III, the reduction of mechanical parameters was not considered. The magnitude of displacement vectors and joint shear displacement were slightly smaller than those in Scenario I (Figs. 10c and 12c). As shown in Table 2, the sums of W_{50} for C3~C7 was 3 m, 9 m, and 15 m smaller than the values in Scenario I. For elevations of 561 m and 695 m, the valley contraction was, respectively, 73.7 mm and 73.4 mm, which was smaller than the values in Scenario I. The magnitude decreased by 15.6% (13.6 mm) and 9.1% (7.3 mm), compared with Scenario I. This difference indicated that the reduction of shear

mechanical properties induced by water–rock interactions could partly explain the reason for the valley contraction.

In Scenario IV, the reduction of normal stiffness was considered. The magnitude of displacement vectors, joint shear displacement, and W_{50} of C3–C7 were similar to those in Scenario II, and these values were larger than those in Scenario I and II (Fig. 12d). For survey lines with elevations of 561 m and 695 m, the valley contraction was 95.5 and 85.8 mm, respectively. Compared with Scenario I, the valley contraction increased by 9.4% (8.2 mm) and 6.3% (5.1 mm). Note that the distribution of α was the same in Scenario I and IV. However, the difference of joint slip and X-displacement indicated that the reduction of normal stiffness had a notable influence on the valley contraction.

In both Scenarios II and IV, the overestimate of α and the reduction of normal stiffness mainly changed the normal mechanical behavior of rock fractures. For Scenario II, the treatment of $\alpha = 1$ decreased the effective stress along rock fractures. For Scenario IV, the weakening of normal stiffness decreased the normal component of stress increment

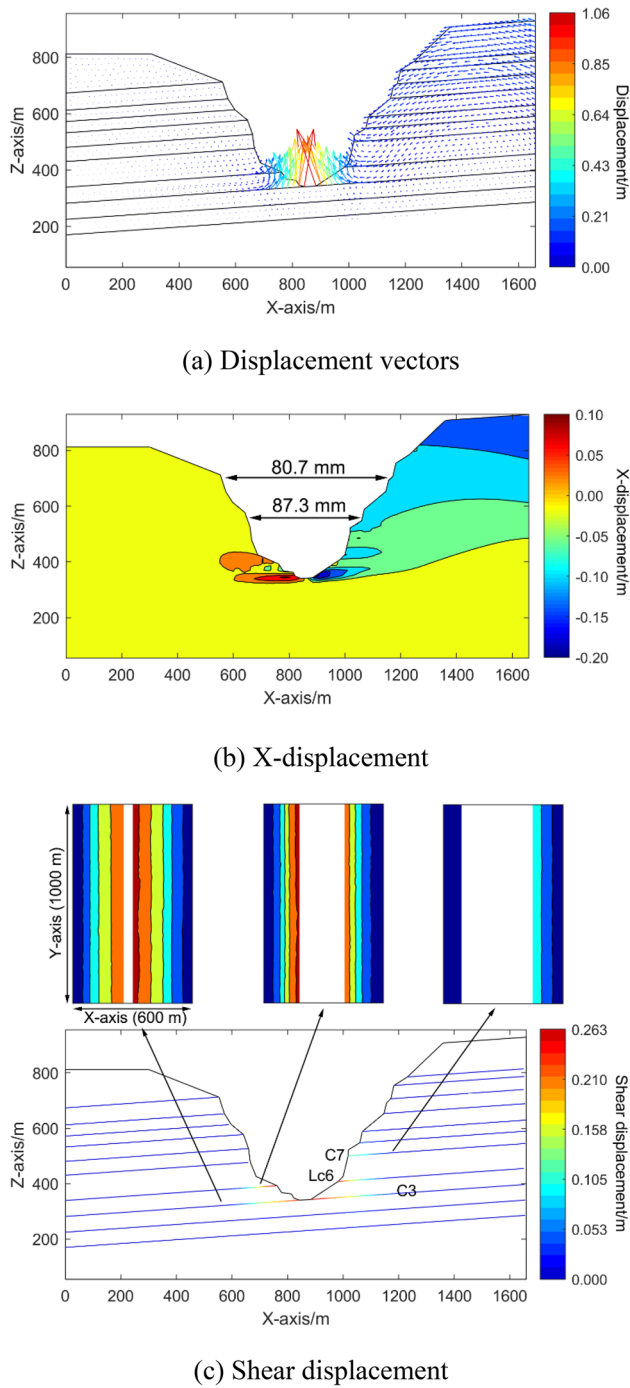


Fig. 8 Displacement vectors, X-displacement of rock mass, and shear displacement of discontinuities in Scenario I

and increased the risk of joint slip based on Eqs. (4) and (5). From the comparison between Scenario II and IV, the similarity of rock matrix displacement and joint slip indicated

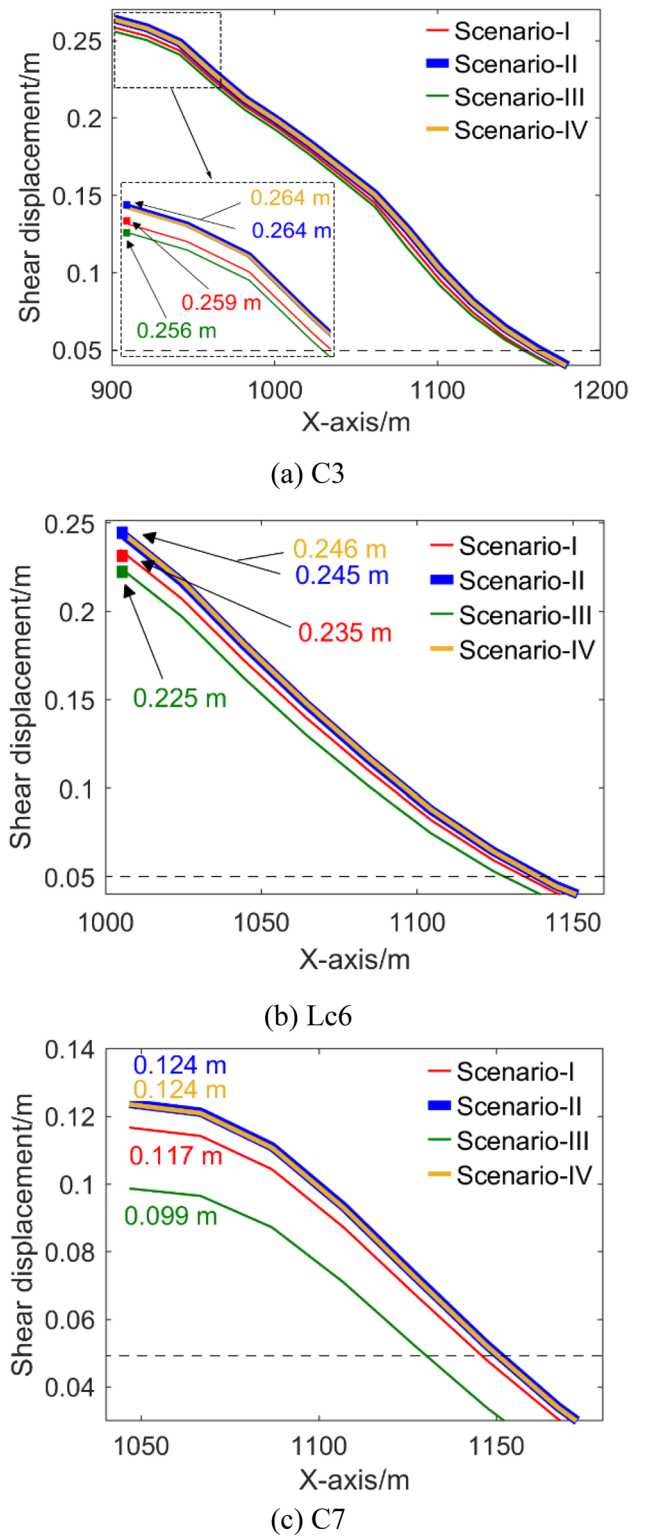


Fig. 9 Shear displacement of discontinuities C3, Lc6, C7 in right bank (dashed lines represent the shear displacement of 0.05 m for defining key segments)

Table 2 Coordinates and lengths of key segments

Fault	Scenario I	Scenario II	Scenario III	Scenario IV
C3-left bank	651 ~ 856 (205)	649 ~ 856 (207)	651 ~ 856 (205)	649 ~ 856 (207)
C3-right bank	902 ~ 1155 (253)	902 ~ 1163 (261)	902 ~ 1152 (250)	902 ~ 1161 (259)
Lc6-left bank	647 ~ 780 (133)	645 ~ 780 (135)	650 ~ 780 (130)	646 ~ 780 (134)
Lc6-right bank	1005 ~ 1135 (130)	1005 ~ 1140 (135)	1005 ~ 1129 (124)	1005 ~ 1139 (134)
C7	1047 ~ 1144 (97)	1047 ~ 1150 (103)	1047 ~ 1129 (82)	1047 ~ 1149 (102)

Note: the numbers outside the parenthesis are the coordinates of the key segments, and the numbers inside the parenthesis are the length of the key segments

that change of normal mechanical properties and stress state played an important role in valley contraction.

4 Discussion

4.1 Mechanism of Valley Contraction Subjected to Water–Rock Interaction

To understand the effects of water–rock interactions on deformation behavior of fractured reservoir bank slope, Mohr circle diagram is used to compare the fracture stress states under varying water levels (Fig. 13). For the representative measurement point m1 on the fracture Lc6 below the water level of 560 m (Fig. 13b), the changing position (lateral translation) and diameter (expansion) of the Mohr circle before and after impoundment indicate that the fracture Lc6 experiences a combined effect of water pressure elevation and ambient stress change. In addition, the changing strength line due to water–rock chemical interaction induces the weakening of the fracture Lc6. Therefore, water pressure elevation, ambient stress change, and mechanical parameter weakening during impoundment are the main reasons of slippage of the fracture Lc6.

For the representative measurement point m2 on the fracture C8 that is between the water levels of 560 m and 600 m (Fig. 13c), the changing position (lateral translation) of the Mohr circles before and after impoundment is observed, while the diameter of the Mohr circles does not change before and after impoundment. This indicates that the fracture C8 only experiences the effect of water pressure elevation. In addition, the changing strength line due to water–rock physical interaction induces the weakening of the fracture C8. Therefore, water pressure elevation and mechanical parameter weakening during impoundment are the main reasons of slippage of the fracture C8.

Comparing the two measurement points m1 and m2, it is found that the lower fractures experience more significant changes in their stress states and mechanical properties during impoundment. Those fractures play a more important role in determining the deformation behavior of fractured reservoir bank slope. In this study, the effective

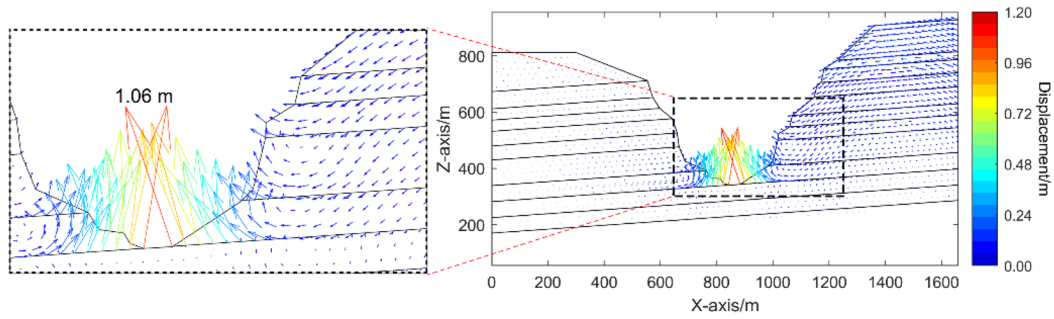
stress coefficient is considered to compute the water–rock mechanical interaction. Figure 13b and c shows that $\alpha = 1$ may overestimate the effect of water pressure elevation, and induce some errors in predicting deformation magnitude of fractured reservoir bank slope during impoundment, especially for those key fractures at a low elevation.

When there are weak layers/zones/structures in the reservoir bank slopes and dam foundations, they may cause the significant valley contraction after impoundment. In addition to install sufficient monitoring points on reservoir slope surfaces, monitoring points should also be arranged in those weak layers/zones/structures. Of course, efficient control methods may be employed to slow down the weakening rate of those weak layers/zones/structures caused by water–rock chemical interactions during long-term operation.

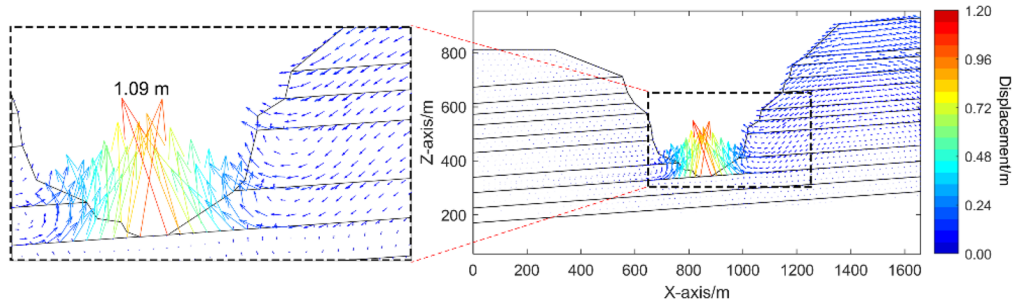
4.2 Comparison with Previous Studies

For the reservoir under analysis, the change of water level could induce the change of mechanical properties and stress state of rock fractures. For the rock fractures under water level, the immersion led to complex physicochemical process to weaken the mechanical behavior of rock fractures. In the past studies, the difference between wet and dry rock fractures was treated by assigning two series of mechanical parameters in two different scenarios, and the effect of physicochemical process was demonstrated by comparing the two scenarios (Zhao et al. 2018; Ning et al. 2021; Gu and Huang 2016; Zhang et al. 2012). However, the constant mechanical parameters of wet rock fractures neglected the relation between immersion duration and the reduction of mechanical parameters. In this study, the continuous reduction in mechanical properties of wet rock fractures below water level of 560 m with time was successfully considered based on the empirical expression in Dou et al. (2021).

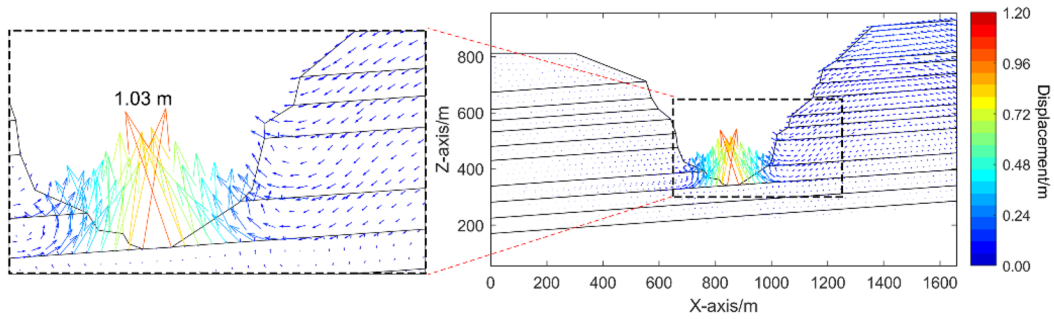
For numerical simulation of coupled hydro-mechanical behavior, $\alpha = 1$ is usually considered when calculating effective stress in rock fracture or rock matrix (Cappa et al. 2008; Li et al. 2016; Chen et al. 2018; Zhao et al. 2018; Liu et al. 2023b; Shui et al. 2021). In fact, α might be smaller than 1 for actual rock fractures in indoor experiments, and it is strongly related to the stress state and deformation behavior,



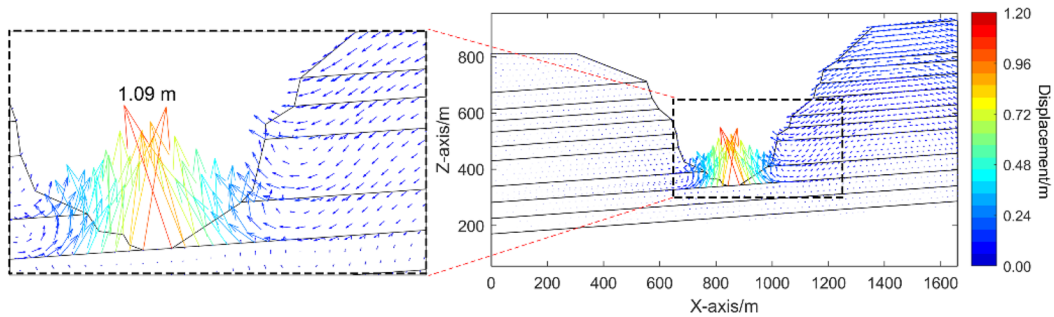
(a) Scenario I



(b) Scenario II



(c) Scenario III



(d) Scenario IV

Fig. 10 Displacement vectors of rock mass in Scenario I–IV (maximum displacement magnitudes are indicated)

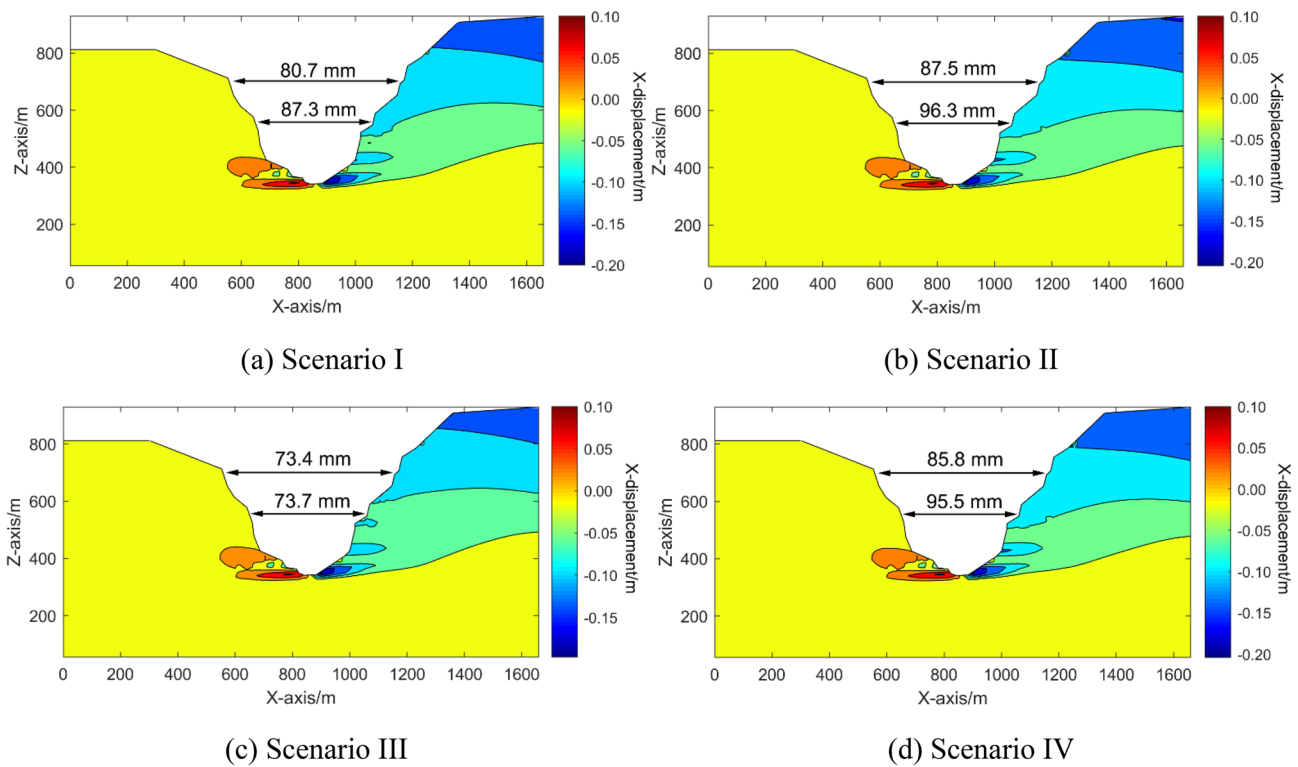


Fig. 11 Horizontal displacement of rock mass in Scenario I–IV (valley contractions in the elevations of 561 m and 695 m are indicated for easy comparison among different scenarios)

which indicated that this value could change according to external pressure on rock fractures (Dassanayake et al. 2015; Chen et al. 2018; Cheng et al. 2022). Therefore, $\alpha = 1$ might cause the overestimation of deformation of rock mass and increased the cost of support systems. Instead of $\alpha = 1$, this study employed a practical expression of α into the simulation of bank slopes (Zhao et al. 2021).

Li et al. (2023b) used poroelastic, thermo-poroelastic, poroelastic-plastic, and poroelastic-creep models to study the valley deformation process of the Xiluodu dam before and after impoundment, and found that the creep of the basalt formation is the leading cause of valley contraction. In their models, the creep parameters were changed after reservoir impoundment. In our DEM models, reductions in shear parameters of rock fractures caused by water–rock chemical reactions are considered. In fact, changes in creep parameters in continuum-based models and shear parameters of rock fractures in DEM models essentially represent the same mechanism. At present, temperature effect on valley contraction still remains controversial (Jiang et al. 2020; Li et al. 2023b), and more studies are needed in future.

4.3 Limitations

For water–rock physical and chemical interactions, this study mainly focused on the reductions in shear parameters of rock

fractures. However, some studies showed that long-term immersion also has weakening effects on other mechanical parameters. Miao et al. (2016) conducted a 60-day immersion experiment (distilled water and NaCl solution with pH = 7) on intact rock, and showed that Young's modulus decreased by 10%–20% after immersion treatment. Qiao et al. (2016) showed that Young's modulus of intact rock could decrease by 37.7% after 180 days' immersion in distilled water. For Scenario IV in Sect. 3.3, both normal stiffness and shear stiffness of rock fractures were weakened, and the ratio of normal stiffness to shear stiffness was assumed to be constant. The difference between Scenarios I and IV in Sect. 3.3 indicated that the reduction in normal stiffness had a notable influence on valley deformation. In addition, the product of u_{nmax} and k_{n0} was assumed to be a certain value without supporting of experimental data. Therefore, more experiments are needed to determine the material parameters of basalt fractures in the Xiluodu dam site. Considering the uncertainty in material parameters and initial conditions, more parametric studies are required on the parameters of rock and discontinuities and initial conditions.

Although the valley contractions are almost the same at the upstream and downstream locations (Li et al. 2023b), and 2D model may be reasonable to study the deformation behavior of fractured reservoir bank slopes where the arch dam is not included. In fact, the present results show that

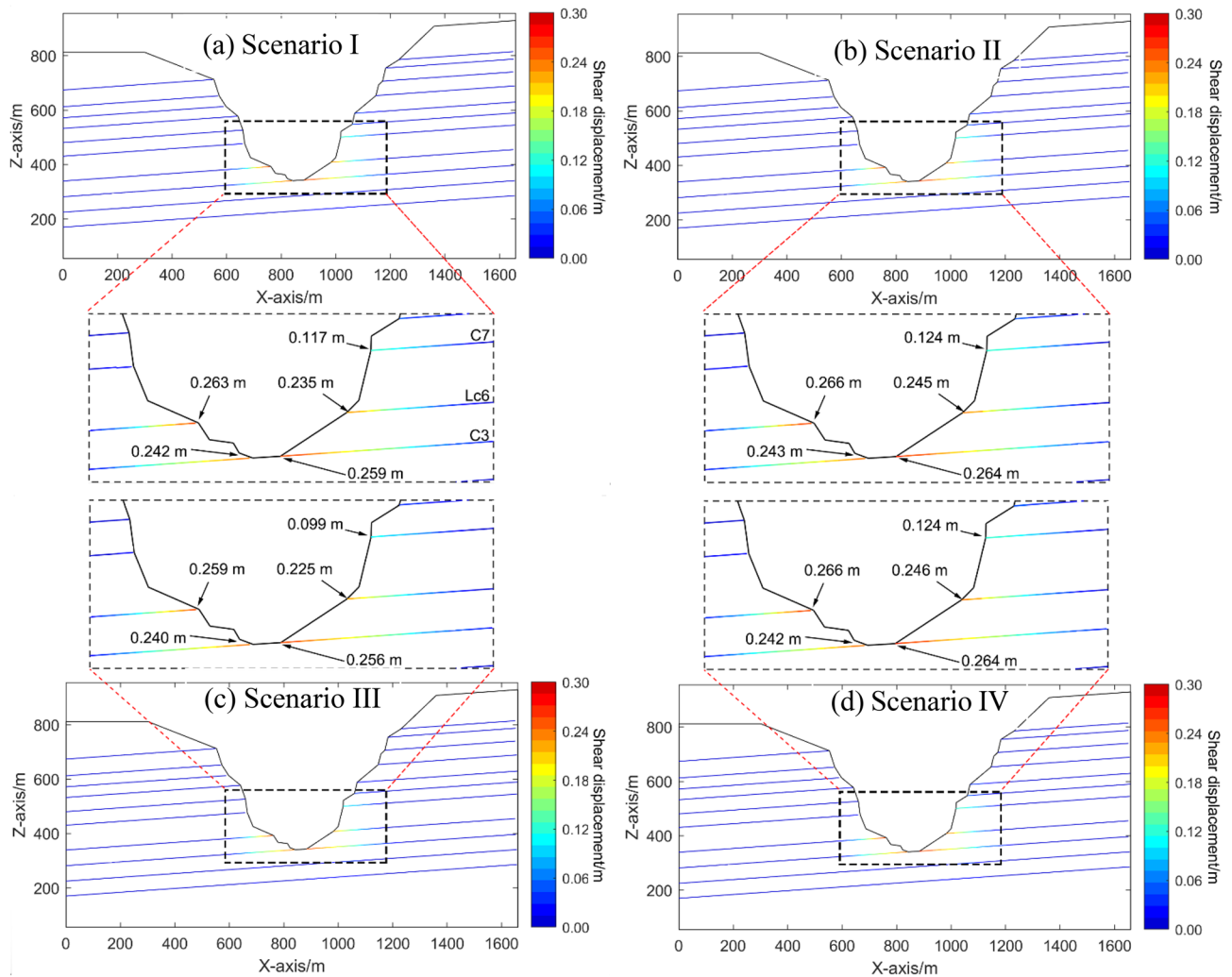


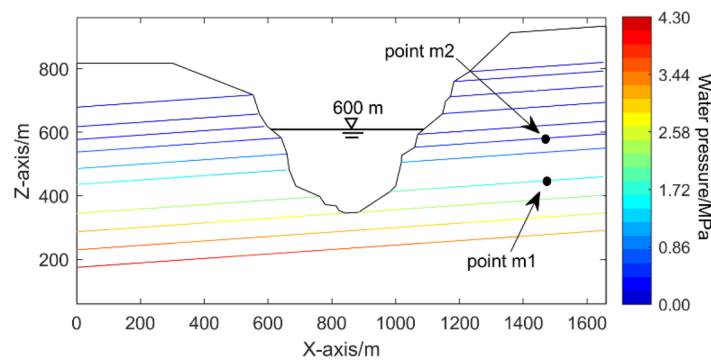
Fig. 12 Shear displacement of discontinuities in Scenario I–IV (maximum shear displacements along C3, Lc6, and C7 are indicated)

different sections have different valley contraction values, and thus, 3D models are necessary in this study. In the adopted DEM model, the arch dam was not considered due to computational restrictions. Future studies should be carried out to assess the relevance of the dam/reservoir interaction during impoundment. The present DEM model can be easily extended to consider the interactions between the arch dam and the reservoir slopes. Compared with the far-field and regional-scale models of the Xiluodu dam site (Chen et al. 2023; Li et al. 2023b), the present DEM is relatively small, and some important, such as karstification in the limestone formation, groundwater exchange between confined and unconfined aquifer systems, and tectonic stresses, are not well considered. In addition, the boundary conditions are artificially assigned due to small size of DEM models. Therefore, multi-scale DEM models are strongly recommended in future studies to overcome the above problems. Nonlinear constitutive models of rock fractures and effects

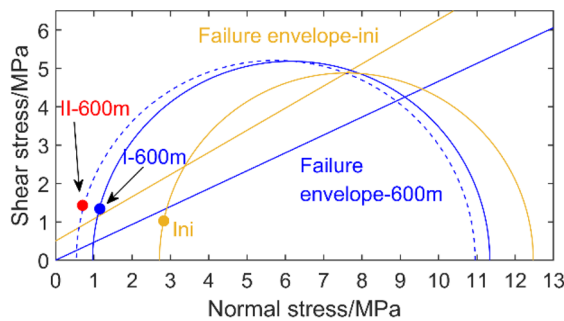
of rough fracture surfaces and infilling materials may also be attempted in future studies.

5 Conclusion

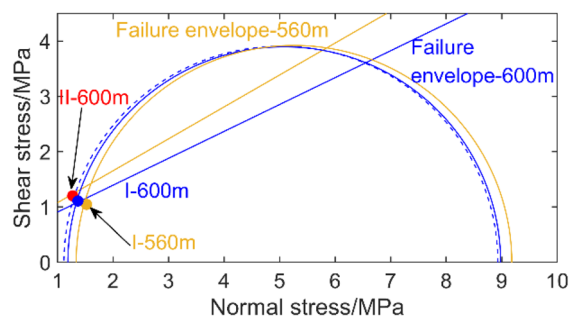
During impoundment, the monitoring and controlling of valley deformation plays an important role in safety of high arch dams, but the mechanisms of valley deformation were poorly understood due to the complexity of the coupled hydro-mechanical behavior of fractured reservoir bank slopes. In this numerical study, the effects of mechanical, physical and chemical water–rock interactions on deformation and stability of fractured reservoir bank slopes were examined using three-dimensional DEM, based on a case study of valley deformation at the Xiluodu Hydropower Station. The main concluding remarks are drawn below:



(a) Positions of m1 and m2



(b) m1



(c) m2

Fig. 13 Comparison of stress state of m1 ~ m2 under the water level of 560 m and 600 m. The yellow line and yellow semicircle represent the failure envelope and Mohr circle before impoundment, while the

blue line, blue solid semicircle, and blue dashed semicircle represent failure envelope, Mohr circles in Scenario I (I-600 m) and Mohr circles in Scenario II (II-600 m) under the water level of 600 m

1. Mechanical, physical, and chemical water–rock interactions in rock fractures are incorporated into discrete element modeling of fractured reservoir bank slopes based on effective stress coefficient in rock fractures and empirical models, which is verified using the monitoring data of valley contraction in the Xiluodu dam.
2. Four scenarios are designed to understand the role of mechanical, physical, and chemical water–rock interactions on deformation of fractured reservoir bank slopes, and the slip of shear zones due to water pressure elevation and mechanical parameter weakening is the main reason of impoundment-induced valley contraction.
3. Compared with the conventional hydro-mechanical models of rock fractures, the effective stress coefficient is used to accurately calculate the water–rock mechanical interaction in rock fractures, and empirical models are used to describe immersion-induced degradation in shear parameters. More experimental studies are needed to provide material parameters for these new developments.

Acknowledgements This work is supported by the National Natural Science Foundation of China (U2067203, 42277140) and Tsinghua University Initiative Scientific Research Program (2022Z11QYJ006).

Data availability statement Data supporting this study can be requested from the authors.

References

Barla G, Antolini F, Barla M, Mensi E, Piovano G (2010) Monitoring of the Beaugard landslide (Aosta Valley, Italy) using advanced and conventional techniques. *Eng Geol* 116:218–235

Biot MA (1941) General theory of three-dimensional consolidation. *J Appl Phys* 12:155–164

Cappa F, Guglielmi Y, Rutqvist J, Tsang CF, Thoraval A (2008) Estimation of fracture flow parameters through numerical analysis of hydromechanical pressure pulses. *Water Resour Res* 44:W11408

Chen Y-F, Ren W, Yang Z, Hu R, Miao Y-P, Zhou C-B (2023) Evaluation of basin-scale hydrogeological changes induced by reservoir operation at the Xiluodu dam site. *J Hydrol* 620:129548

Cheng L, Liu YR, Yang Q, Pan YW, Lv Z (2017) Mechanism and numerical simulation of reservoir slope deformation during

- impounding of high arch dams based on nonlinear FEM. *Comput Geotech* 81:143–154
- Cheng Z, Chen Z, Dong W, Hu D, Zhou H (2022) Effects of fracture filling ratio and confining stress on the equivalent effective stress coefficient of rocks containing a single fracture. *Int J Rock Mech Min Sci* 160:105239
- Dassanayake ABN, Fujii Y, Fukuda D, Kodama J (2015) A new approach to evaluate effective stress coefficient for strength in Kimachi sandstone. *J Petrol Sci Eng* 131:70–79
- Dou Z, Gao T, Zhao Z, Li J, Yang Q, Shang D (2020) The role of water lubrication in critical state fault slip. *Eng Geol* 271:105606
- Dou Z, Gao T, Zhao Z, Li J, Yang Q, Yi S (2021) Effect of immersion duration on shear behavior of granite fractures. *Rock Mech Rock Eng* 54:4809–4823
- Espada M, Muralha J, Lemos JV, Jiang Q, Feng X-T, Fan Q, Fan Y (2018) Safety analysis of the left bank excavation slopes of Baihetan arch dam foundation using a discrete element model. *Rock Mech Rock Eng* 51:2597–2615
- Fan L, Yu M, Wu A, Zhang Y (2022) Developing an in situ, hydro-mechanical coupling, true triaxial rock compression tester and investigating the deformation patterns of reservoir bank slopes. *Q J Eng GeolHydrogeol* 55:2021–2043
- Farinha MLB, de Lemos JV, Maranha Das Neves E. Analysis of foundation sliding of an arch dam considering the hydromechanical behavior. *Frontiers of Structural and Civil Engineering* 2012, 6: 35–43.
- Gu D, Huang D (2016) A complex rock topple-rock slide failure of an anaclinal rock slope in the Wu Gorge, Yangtze River. *China Engineering Geology* 208:165–180
- Jiang H, Zhang C-H, Zhou Y-D, Pan J-W, Wang J-T, Wu M-X, Fan Q-X (2020) Mechanism for large-scale canyon deformations due to filling of large reservoir of hydropower project. *Sci Rep* 10:12155
- Kim T, Jeon S (2019) Experimental study on shear behavior of a rock discontinuity under various thermal, hydraulic and mechanical conditions. *Rock Mech Rock Eng* 52:2207–2226
- Li Y, Chen YF, Zhou CB (2016) Effective stress law for partially saturated rock fractures. *Rock Mech Rock Eng* 49:1091–1096
- Li B, Ye X, Dou Z, Zhao Z, Li Y, Yang Q (2020) Shear strength of rock fractures under dry, surface wet and saturated conditions. *Rock Mech Rock Eng* 53:2605–2622
- Li M, Zhou Z, Zhuang C, Zhou Z (2022) Deformation mechanism and model of river valley contraction of the Xiluodu reservoir. *China Environmental Earth Sciences* 81:491
- Li B, Xu J, Xu W, Wang H, Yan L, Meng Q, Xie W-C (2023a) Mechanism of valley narrowing deformation during reservoir filling of a high arch dam. *Eur J Environ Civ Eng* 27:2411–2421
- Li M, Selvadurai APS, Zhou Z (2023b) Observations and computational simulation of river valley contraction at the Xiluodu dam, Yunnan. *China Rock Mechanics and Rock Engineering* 56:4109–4231
- Liu X, Tang C, Li L, Lv P, Sun R (2018) Microseismic monitoring and stability analysis of the right bank slope at Dagangshan hydropower station after the initial impoundment. *Int J Rock Mech Min Sci* 108:128–141
- Liu Y, Wang W, He Z, Lyv S, Yang Q (2020) Nonlinear creep damage model considering effect of pore pressure and analysis of long-term stability of rock structure. *Int J Damage Mech* 29:144–165
- Liu B, Meng W, Zhao Z, Lin T, Zhang J (2023a) Coupled thermal-hydro-mechanical modeling on characteristics of excavation damage zone around deep tunnels crossing a major fault. *Tunn Undergr Space Technol* 134:105008
- Liu Y, Hu Z, Xu T et al (2023b) Discrete element modeling for the multistage hydraulic stimulation of a horizontal well in hot dry rock. *Comput Geotech* 156:105274
- Londe P (1987) The Malpasset dam failure. *Eng Geol* 24:295–329
- Miao S, Cai M, Guo Q, Wang P, Liang M (2016) Damage effects and mechanisms in granite treated with acidic chemical solutions. *Int J Rock Mech Min Sci* 88:77–86
- Itasca Consulting Group Inc. 3DEC - three dimensional distinct element code version 5.2 user's guide. Minneapolis, MN. 2016.
- Müller-Salzburg L (1987) The Vajont catastrophe - A personal review. *Eng Geol* 24:423–444
- Ning Y, Tang H, Zhang G, Smith JV, Zhang B, Shen P, Chen H (2021) A complex rockslide developed from a deep-seated toppling failure in the upper Lancang River. *Southwest China Engineering Geology* 293:106329
- Paronuzzi P, Rigo E, Bolla A (2013) Influence of filling-drawdown cycles of the Vajont reservoir on Mt. Toc Slope Stability Geomorphology 191:75–93
- Pellet FL, Keshavarz M, Boulon M (2013) Influence of humidity conditions on shear strength of clay rock discontinuities. *Eng Geol* 157:33–38
- Pirzada MA, Roshan H, Sun H, Oh J, Andersen MS, Hedayat A, Bahaaddini M (2020) Effect of contact surface area on frictional behavior of dry and saturated rock joints. *J Struct Geol* 135:104044
- Qiao L, Wang Z, Huang A (2016) Alteration of mesoscopic properties and mechanical behavior of sandstone due to hydro-physical and hydro-chemical effects. *Rock Mech Rock Eng* 50:255–267
- Shang D, Zhao Z, Dou Z, Yang Q (2020) Shear behaviors of granite fractures immersed in chemical solutions. *Eng Geol* 279:105869
- Sun G, Lin S, Cheng S, Sui T, Li C, Zheng H (2018) Mechanisms of interaction between an arch dam and abutment slope using physical model tests. *Rock Mech Rock Eng* 51:2483–2504
- Sun M, Xu W, Wang H, Meng Q, Yan L, Xie W-C (2020) A novel hybrid intelligent prediction model for valley deformation: a case study in Xiluodu Reservoir Region, China. *Computers, Materials and Continua* 66:1057–1074
- Sun L, Tang X, Abdelaziz A, Liu Q, Grasselli G. Stability analysis of reservoir slopes under fluctuating water levels using the combined finite-discrete element method. *Acta Geotechnica* 2023. (In press)
- Wang S, Liu Y, Yang Q, Wang X (2020) Analysis of the abutment movements of high arch dams due to reservoir impoundment. *Rock Mech Rock Eng* 53:2313–2326
- Wu A, Xiang LF, Fu X, Zhang Y, Zhong Z, Yu M (2021) Design and application of hydro-mechanical coupling test system for simulating rock masses in high dam reservoir operations. *Int J Rock Mech Min Sci* 140:104638
- Xia M, Ren GM, Li TB, Cai M, Yang TJ, Wang ZL (2019) Complex rock slope deformation at Laxiwa hydropower station, China: background, characterization, and mechanism. *Bull Eng Geol Env* 78:3323–3336
- Xiong X, Shi Z, Xiong Y, Peng M, Ma X, Zhang F (2019) Unsaturated slope stability around the Three Gorges Reservoir under various combinations of rainfall and water level fluctuation. *Eng Geol* 261:105231
- Xu L, Rong G, Qiu Q, Zhang H, Chen W, Cheng Z. Analysis of reservoir slope deformation during initial impoundment at the Baihetan Hydropower Station, China. *Engineering Geology* 2023, 107201. (in press)
- Yang J, Zhao X, Song S, Du X, Wu F, Zou Q (2022a) Distribution characteristics of valley stress of hydropower engineering projects in western Sichuan. *Bull Eng Geol Env* 81:156
- Yang X, Ren X, Ren Q (2022b) Study on influence of construction and water storage process on valley deformation of high arch dam. *Bull Eng Geol Env* 81:259
- Yin Y, Huang B, Wang W, Wei Y, Ma X, Ma F, Zhao C (2016) Reservoir-induced landslide and risk control in three Gorges project on Yangtze River, China. *Journal of Rock Mechanics and Geotechnical Engineering* 8:577–595

- Yin Z, Huang H, Zhang F, Zhang L, Maxwell S (2020) Three-dimensional distinct element modeling of fault reactivation and induced seismicity due to hydraulic fracturing injection and back-flow. *Journal of Rock Mechanics and Geotechnical Engineering* 12:752–767
- Zhang M, Dong Y, Sun P (2012) Impact of reservoir impoundment-caused groundwater level changes on regional slope stability: a case study in the Loess Plateau of Western China. *Environmental Earth Sciences* 66:1715–1725
- Zhao Z, Yang J, Zhang D, Peng H (2017a) Effects of wetting and cyclic wetting-drying on tensile strength of sandstone with a low clay mineral content. *Rock Mech Rock Eng* 50:485–491
- Zhao Z, Yang J, Zhou D, Chen Y (2017b) Experimental investigation on the wetting-induced weakening of sandstone joints. *Eng Geol* 225:61–67
- Zhao Z, Guo T, Ning Z, Dou Z, Dai F, Yang Q (2018) Numerical modeling of stability of fractured reservoir bank slopes subjected to water-rock interactions. *Rock Mech Rock Eng* 51:2517–2531
- Zhao Z, Chen S, Chen Y, Yang Q (2021) On the effective stress coefficient of single rough rock fractures. *Int J Rock Mech Min Sci* 137:104556
- Zhou Z, Zhou Z, Li Y, Vanapalli SK, Huang H (2022) Analysis of deformation and leakage performance of Xiluodu reservoir dam foundation using a coupled two-factor stress-deformation-seepage model. *Eng Geol* 310:106871
- Zhou C-B, Chen Y-F, Hu R, Yang Z (2023) Groundwater flow through fractured rocks and seepage control in geotechnical engineering: Theories and practices. *J Rock Mech Geotech Eng* 15:1–36
- Zhuang W, Liu Y, Zhang R, Hou S, Yang Q. Study on deformation mechanism and parameter inversion of a reservoir bank slope during initial impoundment. *Acta Geotechnica* 2023. (in press)

Publisher's Note Springer Nature remains neutral with regard to jurisdictional claims in published maps and institutional affiliations.

Springer Nature or its licensor (e.g. a society or other partner) holds exclusive rights to this article under a publishing agreement with the author(s) or other rightsholder(s); author self-archiving of the accepted manuscript version of this article is solely governed by the terms of such publishing agreement and applicable law.